WORLD METEOROLOGICAL ORGANIZATION

GLOBAL ATMOSPHERE WATCH

No. 10 – JULY 2026

WMO AIRBORNE DUST BULLETIN

Overview of global airborne dust concentrations in 2025

Overall, the global dust conditions in 2025 were similar to those in 2024. The global annual mean surface dust concentration in 2025 was 12.1 μg m^{-3}, slightly lower than the 12.5 μg m^{-3} reported in 2024 (*WMO Airborne Dust Bulletin, No. 9*). The highest annual mean dust concentrations worldwide (~800–1 100 μg m^{-3}) remained centred in the Bodélé Depression in Chad (Figure 1, left), one of the world's most active dust source regions. Compared with 2024, enhanced dust activity was observed over parts of Iraq and Kuwait, the Taklamakan Desert and Central Asia, including the Karakum and Kyzylkum Deserts. These regional increases coincided with more pronounced drought conditions across parts of Asia during 2025, whereas severe drought conditions in 2024 were more prominent over the Maghreb region.[1] In the southern hemisphere, the highest surface dust concentrations (~150–300 μg m^{-3}) occurred over central Australia and the west coast of South Africa.

Dust emitted from major source regions is transported over distances of hundreds to thousands of kilometres, affecting large downwind areas. Regions frequently influenced by long-range dust transport include the tropical North Atlantic, the Caribbean, South America, the Mediterranean, the Arabian Sea, the Bay of Bengal and eastern China. African dust transport affected parts of the Caribbean and Europe in 2025, although transport intensity was generally lower than in 2024.

Relative to the 1981–2010 climatology, dust concentrations in 2025 were generally below average across northern Africa and western Asia (Figure 1, right). Notable exceptions included the Red Sea, the Persian Gulf, the Arabian Sea, parts of West and Central Africa, Afghanistan, Pakistan, India, the Bay of Bengal, Central Asia, the Taklamakan Desert and north-central China, where above-average dust concentrations were recorded.

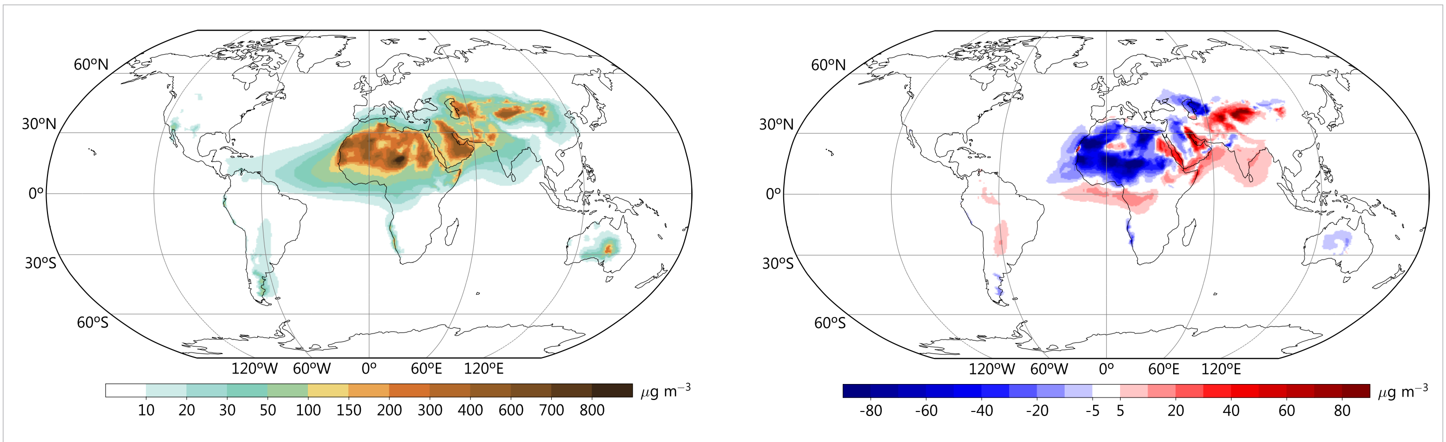

Figure 1. Left: Annual mean surface dust concentration (in μg m^{-3}) in 2025. Right: Anomaly of the annual mean surface dust concentration (in μg m^{-3}) in 2025 relative to the 1981–2010 mean.

Source: National Aeronautics and Space Administration (NASA) Modern-Era Retrospective Analysis for Research and Applications, Version 2 (MERRA-2) dataset. Third-party map. This map was provided by the China Meteorological Administration (CMA) on 15 May 2026 and may not fully align with United Nations and WMO map guidance.

1 See the Standardised Precipitation-Evapotranspiration Index (SPEI) Global Drought Monitor.

Major sand and dust storm events in 2025

North Africa and the Middle East

Between March and May 2025, North Africa and the Middle East were hit by a series of major dust storms.

The first major event occurred between 30 March and 2 April (Figure 2, row one), when a Mediterranean cold front collided with hot Saharan air over Algeria, Tunisia and Libya. Strong winds lifted large amounts of dust, especially over eastern Algeria and western Libya, reducing visibility to 2 500 m. As the storm moved east

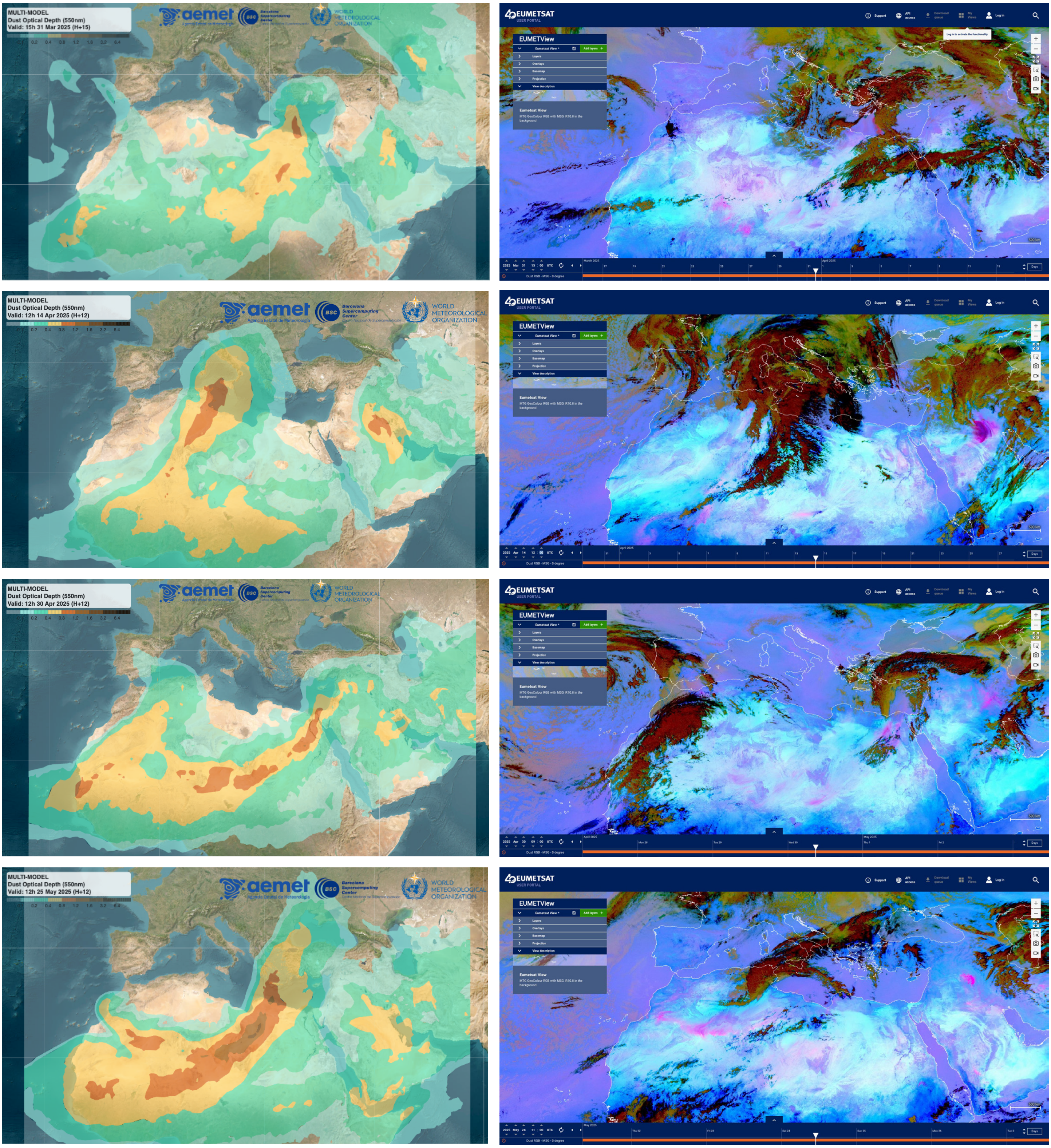

Figure 2. Left: Forecasts of dust optical depth at 550 nm from the Barcelona Dust Regional Center multi-model ensemble system. Right: the SEVIRI Dust RGB product (pink is associated with sand and dust). [Row one:] 1 April, 1200 UTC; [row two:] 14 April, 1200 UTC; [row three:] 30 April, 1200 UTC; [row four:] 25 May, 1200 UTC.

Source: Left: Third-party map. This map was provided by the Barcelona Dust Regional Center on 15 May 2026 and may not fully align with United Nations and WMO map guidance. Right: Third-party map. This map was provided by the European Organisation for the Exploitation of Meteorological Satellites (EUMETSAT) on 15 May 2026 and may not fully align with United Nations and WMO map guidance.

on 31 March, the dust reached Egypt's western coast, including Matruh, where visibility dropped to 1 500 m. By 1–2 April, the dust had spread across all of Egypt, affecting the north-western and southern regions of the country before moving north-east across the Mediterranean. Southern Greece experienced visibility below 5 000 m on 2 April, while in Amman, Jordan, visibility fell to 900 m.

A second major event developed in mid-April, when a wavy polar jet formed a cut-off low over the Black Sea on 12 April (Figure 2, row two). Its associated cold front crossed Iraq on 14 April, creating hazardous conditions which shut down several airports and resulted in nearly 4 000 people seeking treatment at emergency rooms for respiratory problems.[2]

The most intense storm occurred between 28 and 30 April (Figure 2, row three). It formed when a thermal low over south-western Libya combined with strong pressure gradients across North Africa. Persistent south-westerly winds carried dense dust and sand into western Egypt on 29 April. Severe conditions were reported in the Siwa Oasis, where visibility fell below 500 m. On 30 April, the storm spread across Egypt, with visibility in Aswan reduced to approximately 300 m, disrupting road traffic, maritime navigation and airport operations. Cairo and central Egypt were less affected because most of the dust was confined to the lower atmosphere. Aerosol optical depth (AOD) values in western Egypt exceeded 1.2, while hourly concentrations of particulate matter with a diameter of less than 10 µm (PM_{10}) exceeded 5 000 µg m^{-3} in the Farafra Oasis, indicating extremely poor air quality. Due to the severity of the event, the Egyptian government suspended school and university classes on 30 April following warnings from the Egyptian Meteorological Authority. On 1 May, the storm weakened as winds subsided, though dust continued drifting eastward, reaching Crete in the eastern Mediterranean.

Another major dust storm affected North Africa and the eastern Mediterranean in late May (Figure 2, row four). On 23 May, a Khamsin depression generated strong winds and widespread dust over the southern parts of Algeria, Tunisia and Libya, while northern Algeria and northern Tunisia experienced thunderstorms. A cold air mass on 24 May pushed the thermal low eastward, intensifying winds and spreading dust further across Libya. On 25 May, the storm reached western Egypt and extended towards eastern Europe, turning skies hazy over Crete. On 26–27 May, strong north-westerly winds transported the dust into southern Egypt, Sudan, Cyprus and the eastern Mediterranean. Visibility at Hurghada dropped to 1 500 m, while AOD values exceeded 1.5 in parts of Egypt, indicating very high dust concentrations.

East Asia

From 10 to 14 April, influenced by a Mongolian cyclone and the subsequent cold high pressure, extreme gale winds occurred in the southern part of Mongolia and the region north of the Yangtze River in China. As a result, China experienced its most extensive sand and dust storm (SDS) in terms of impact range in the past decade. This SDS event was characterized by high intensity, wide influence and long duration. The strong winds not only caused intense dust emission in the source areas and their surroundings but also transported the dust southward from Mongolia across most of China. Regions in southern and south-western China, which had rarely been affected by such events in the past, were impacted by this event, with large-scale dusty weather occurring in Hong Kong, Special Administrative Region and the provinces of Guangdong, Hainan Island, Sichuan and Guizhou.

During this event, hourly PM_{10} concentrations exceeded 1 000 µg/m^3 in northern parts of China, with some areas reaching as high as 3 000 to 4 000 µg/m^3. In southern cities such as Guangzhou (Figure 3, right), hourly PM_{10} concentrations also surpassed 400 µg/m^3, resulting in severe air pollution. The Beijing Dust Regional Center accurately forecast the occurrence and development of this SDS event (Figure 3, left).

An unusual dust event was observed over East Asia on 30 November 2025, well outside the typical spring dust season. The horizontal extent of the dust plume was visible in geostationary Himawari satellite imagery using

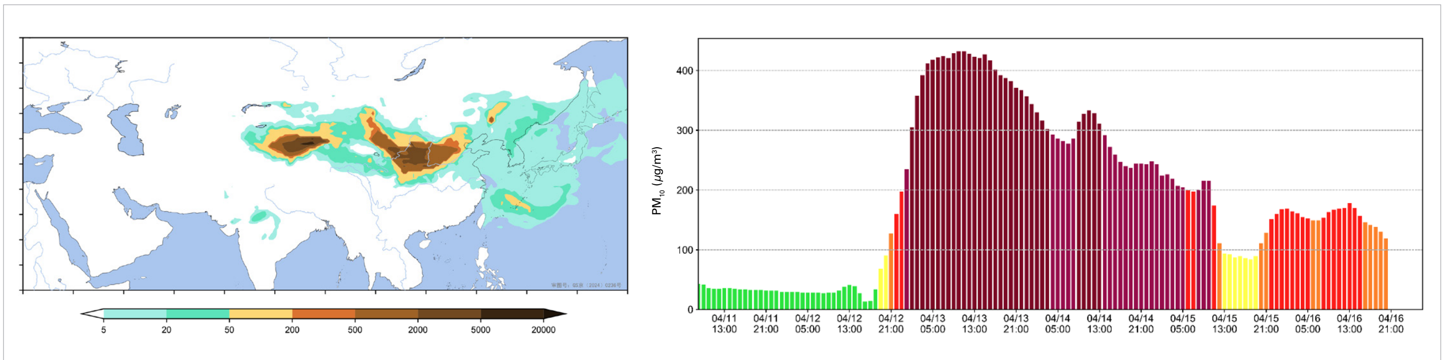

Figure 3. Left: Forecast dust surface concentration (µg/m^3) from the Beijing Dust Regional Center multi-model ensemble system for 11 April 2025, 1500 UTC. Right: PM_{10} monitoring data for Guangzhou, China.

Source: Third-party map. This map was provided by the Beijing Dust Regional Center on 15 May 2026 and may not fully align with United Nations and WMO map guidance.

2 See Dust Storm Sweeps through Iraq.

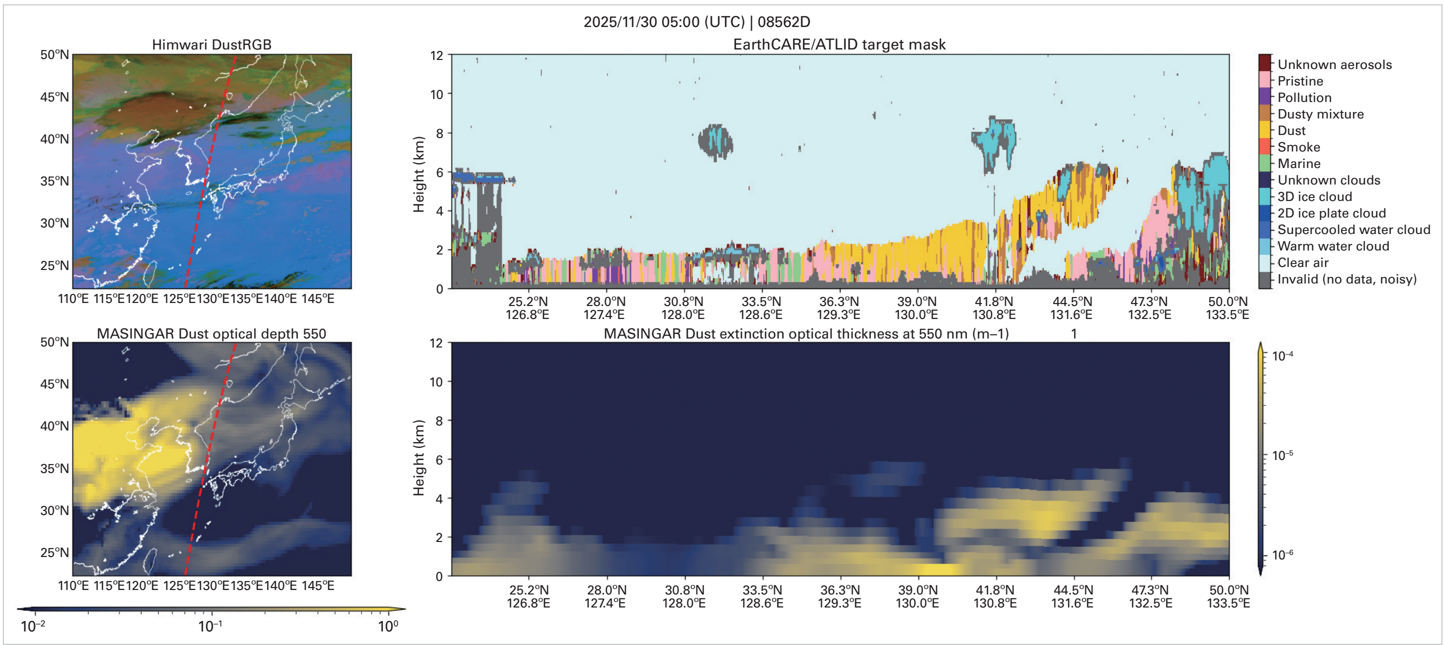

Figure 4. Upper left: Himawari Dust RGB imagery; upper right: ATLID vertical target mask; lower left: forecast dust optical depth at 550 nm by MASINGAR; lower right: forecast vertical dust extinction by MASINGAR, all for the Asian dust event on 30 November 2025. The pink areas on the Dust RGB map indicate dust distribution. The red line on the maps indicates the EarthCARE satellite track.

Source: Third-party images. These images were provided by JMA on 15 May 2026. The maps may not fully align with United Nations and WMO map guidance.

the Dust RGB product (Figure 4, upper left). The Dust RGB imagery showed a broad dust region spreading eastward over the East China Sea towards the Japanese archipelago. During this event, the Atmospheric Lidar (ATLID) onboard the Earth Cloud, Aerosol and Radiation Explorer (EarthCARE) satellite[3] observed a distinct layer of dust transported from East Asia towards Japan. The lidar curtain revealed aerosol layers extending to an altitude of approximately 6 km (Figure 4, upper right), indicating long-range transport from continental source regions. This unseasonal dust transport event was also represented by simulations from the Japanese Meteorological Agency (JMA) forecasting system based on the Model of Aerosol Species in the Global Atmosphere (MASINGAR) (Figure 4, lower images). MASINGAR is one of the forecasting systems included in the Beijing Dust Regional Center model intercomparison. A comparison with ATLID observations showed that MASINGAR successfully reproduced the overall dust distribution and the multilayer structure. However, differences were found in the thickness of the dust layers and their detailed vertical distribution.

North America

The 2025 SDS season in the Chihuahuan Desert border region of Mexico and the United States of America was characterized by exceptionally frequent, intense and long-lasting events, with particularly strong impacts in the Ciudad Juárez, Chihuahua–El Paso, Texas binational metropolitan area. El Paso experienced 50 days with dust weather in 2025, more than double the annual average. The number of dust storms (12) was the highest since 1935, when the USA was in the midst of its protracted "Dust Bowl" disaster. There were more than six hours of continuous SDS conditions in El Paso on 18 March 2025 (Figure 5, left), the longest period of such conditions in Texas in at least 25 years. This event yielded a daily average PM_{10} concentration of 2 064 μg m^{-3} and a daily average concentration of particulate matter with a diameter of less than 2.5 μm ($PM_{2.5}$) of 229 μg m^{-3} in El Paso. Hourly reported PM_{10} concentrations in El Paso on 18 March reached 8 142 μg m^{-3}, the highest hourly concentration measured in Texas since hourly PM monitoring began approximately 27 years ago. The previous record hourly PM_{10} concentration in El Paso was exceeded during eight different events in early 2025.

These dust events had broad health, safety, environmental and economic impacts. Schools, highways and airports were closed temporarily, and public events were postponed in portions of New Mexico, Texas and Chihuahua (see Figure 5, right). Blowing dust and sand contributed to multiple fatal road accidents in the region, including a multi-fatality chain-reaction crash at Lordsburg Playa, New Mexico, one of the deadliest stretches of highway in the USA for dust. The effects of these dust events were felt far beyond the borderlands: PM levels became elevated, and visibility was restricted in the major United States cities of Houston (>1 000 km downwind) and Chicago (>2 000 km downwind) by dust advected from the Chihuahuan Desert during several of the 2025 events. At least six different SDS led to long-distance transport and notable wet deposition of dust thousands of kilometres

3 See https://www.eorc.jaxa.jp/EARTHCARE/about/inst_atlid_e.html.

Figure 5. Sand and dust storms in March 2025 in the USA. Left: Visible image from the National Oceanic and Atmospheric Administration (NOAA) Geostationary Operational Environmental Satellite–19 (GOES-19) on 16 March 2025; right: Photograph of the University of Texas at El Paso campus (USA) on 6 March 2025.

Source: Left: NOAA. Right: Katalina Salas.

downwind, as far away as Ontario (Canada) and the Atlantic coast of the USA. Multidisciplinary teams of researchers from the USA and Mexico are working on understanding the meteorological triggers and land-use factors which caused this extreme dust season.

Ongoing research

Advances in forecasting

Accurate forecasting of dust aerosols remains a major challenge due to the complex interactions between dust life cycles and atmospheric dynamics, as well as the high computational cost of conventional physics based models. Recent advancements in machine learning (ML) and artificial intelligence (AI) have introduced radically new approaches to weather forecasting. By leveraging extensive data availability, such as decades of satellite-based Earth observations, AI models can reconstruct complex atmospheric phenomena with high precision. Although the training phase of ML/AI models can itself be computationally intensive and resource-demanding, once trained, these systems require substantially fewer computational resources for inference and operational forecasting than traditional numerical models, significantly reducing the cost and time associated with routine predictions.

One emerging approach directly uses AI-generated weather forecasts to drive dust models. For example, AI-DUST (Wang and Hua, 2026) combines ML with simplified physical rules to simulate dust emissions and transport without relying on traditional numerical dust modelling systems. This approach shows strong performance in reproducing severe dust events, highlighting the potential of physics-informed AI methods.

Another major development is the use of large AI systems trained on long records of atmospheric data. Gui et al. (2026) developed the AI Global Aerosol–Meteorology Forecasting System (AI-GAMFS) model, which learns global patterns linking weather and dust from decades of NASA MERRA-2 reanalysis data. Once trained, it can produce five-day global dust forecasts within minutes and has shown improved performance compared with several operational systems, especially over East Asia (Figure 6).

Many emerging AI applications for mineral dust forecasting are trained using atmospheric composition reanalysis. While this approach mitigates issues related to observational gaps and sensor inconsistencies, it can also transfer biases and limitations from the underlying reanalysis products to the AI forecasts. A different strategy relies directly on satellite observations rather than long historical datasets.

A recent study developed an AI-based system to forecast atmospheric dust using satellite observations from the Visible Infrared Imaging Radiometer Suite (VIIRS) and weather forecasts from the Global Forecast System (GFS) (covering the period from 2012 to 2024). The model learns from past dust patterns, meteorological conditions, seasonal variability, and terrain, and produces efficient next-day forecasts even when some satellite data are missing. The system was compared with the reference operational system at the Barcelona Dust Regional Center – the MONARCH dust forecasting system, which now also assimilates satellite observations (Figure 7). The results show improved short-term forecasts over Northern Africa, the Mediterranean and the Iberian Peninsula, although near-surface dust concentrations remain more difficult to predict. For longer lead times (up to three days ahead), the AI model performs best for the first day but loses accuracy more quickly than MONARCH.

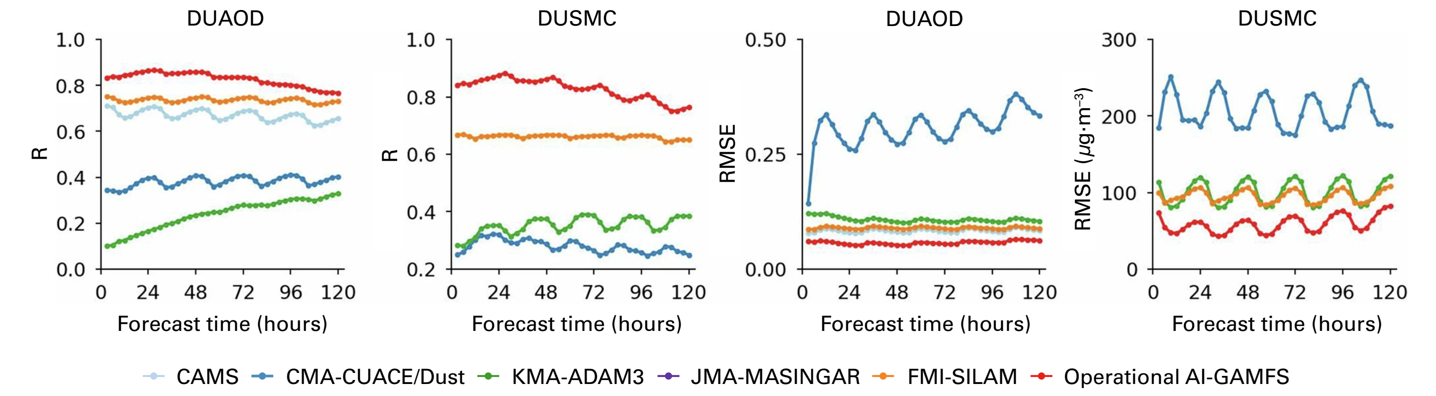

Figure 6. Comparison of five-day forecast accuracy for dust optical depth at 550 nm (DUAOD) and dust surface mass concentration (DUSMC) over East Asia using the NASA MERRA-2 reanalysis as the reference dataset, evaluated using the spatial correlation coefficient (R) and root mean square error (RMSE). This comparison includes AI-GAMFS (initialized by NASA Goddard Earth Observing System Forward Processing (GEOS-FP) analyses), Copernicus Atmosphere Monitoring Service (CAMS), the CMA Chinese Unified Atmospheric Chemistry Environment for Dust (CUACE/Dust) (CMA-CUACE/Dust), ADAM3 from the Korea Meteorological Agency (KMA) Asian Dust Aerosol Model 3 (ADAM-3) (KMA-ADAM3) and SILAM from the Finnish Meteorological Institute (FMI) System for Integrated Modelling of Atmospheric Composition (SILAM) (FMI-SILAM).

Source: Gui et al. (2026)

It captures major dust plumes but may miss smaller secondary events. Future work will focus on improving forecasts beyond 24 hours and integrating additional satellite data, including lidar, to better represent both atmospheric dust and surface-level impacts.

Overall, current results suggest that no single approach performs best for all situations. Some AI systems are better suited for short-lived, rapidly evolving local SDSs, while others perform more consistently for large-scale SDSs that develop and travel over several days.

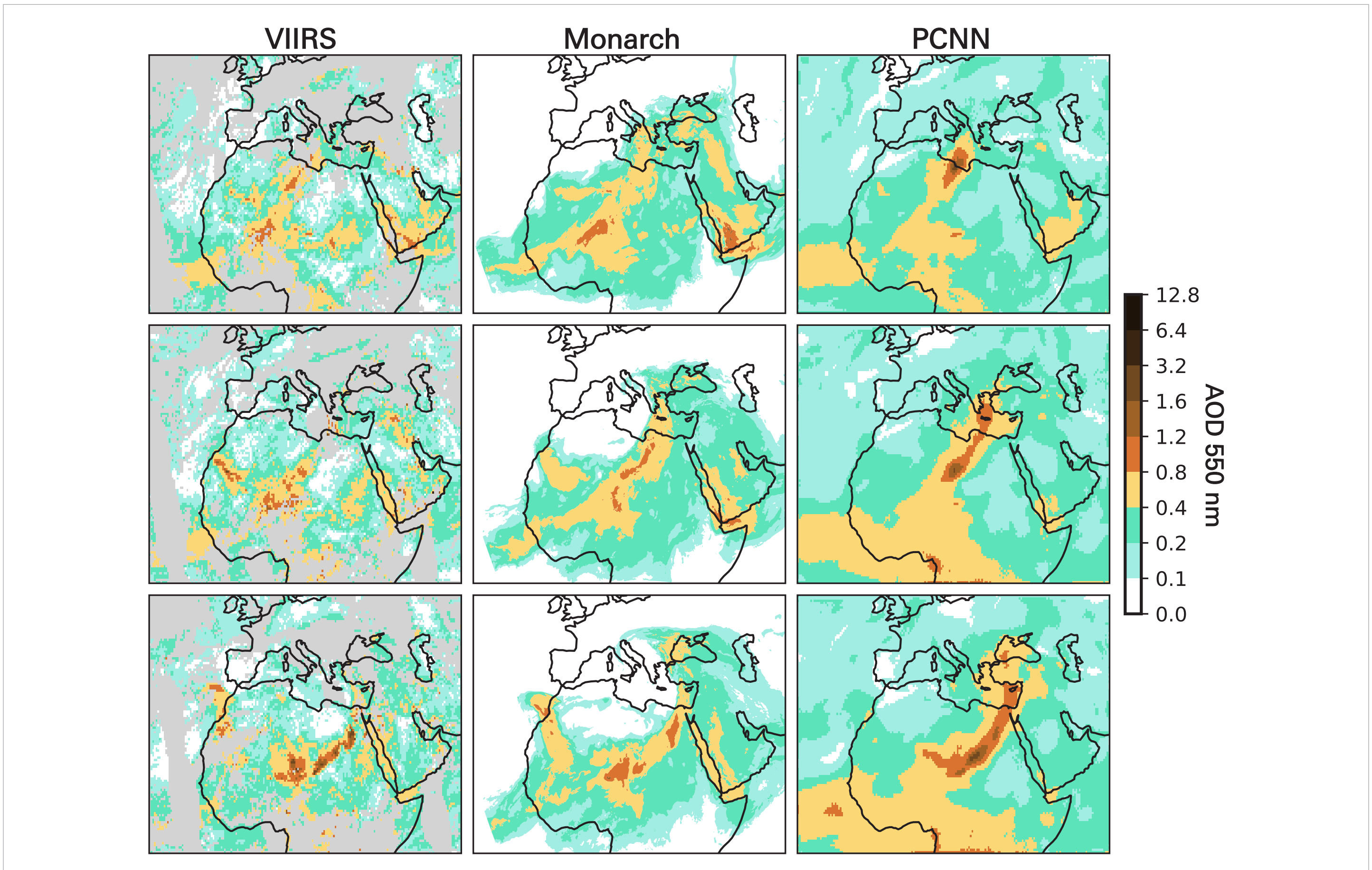

Figure 7. AOD at 550 nm during an episode of dust transport over the Mediterranean for 23–25 March 2025. Top row: 23 March; middle row: 24 March; bottom row: 25 March 2025. Left column: VIIRS satellite observations; centre column: MONARCH forecasts; right column: forecasts by the AI model (partial convolution neural network (PCNN)). Note that the MONARCH maps display the model dust optical depth (DOD) at 550 nm, whereas the other maps display the total AOD at 550 nm.

Source: Third-party map. This map was provided by the Barcelona Supercomputing Center on 15 May 2026 and may not fully align with United Nations and WMO map guidance.

Source monitoring

Monitoring active dust sources (hotspots) involves identifying and tracking both persistent and temporary emission areas, including deserts, dry lake beds, river floodplains and exposed sediments from shrinking or seasonal water bodies. These surfaces can become highly active dust sources when water levels recede, leaving fine sediments vulnerable to wind erosion. Monitoring combines satellite imagery, ground-based observations and numerical models to detect changes in surface conditions, vegetation cover, soil moisture and wind force that control dust emission. This integrated approach helps capture both long-term hotspots and short-lived sources linked to episodic drying events. The resulting hotspot maps provide a spatially explicit basis for identifying priority areas for dust mitigation and land rehabilitation.

Recent advances in satellite remote sensing and analytical methods have significantly improved the identification and mapping of global dust sources. Building on earlier global inventories based on AOD observations from the Moderate Resolution Imaging Spectroradiometer (MODIS), a recent study by Boloorani et al. (2025) developed a new global dust source atlas using Sentinel-5P Absorbing Aerosol Index (AAI) observations for 2018–2024. By combining satellite aerosol products with land-cover, hydrological and soil datasets, the study found that approximately 5% of the Earth's land surface acts as a dust source, mainly concentrated in North Africa (67%) and Asia (30%). Dust sources were classified into desert, vegetation-related and hydrological categories, highlighting the contribution of both natural and anthropogenic processes to global dust emissions.

A study by Al-Hemoud et al. (2024) analysed hotspots in southern Iraq and identified major SDS source areas within the Lower Mesopotamian floodplain, particularly across Al-Muthana and Dhi Qar provinces. MODIS imagery (2000–2021) (see Figure 8), combined with geographic information system (GIS) and ML approaches, was used to delineate dust emission hotspots and associated controlling factors. The hotspot region covers approximately 1 600 km^2, embedded within a broader modelling domain of approximately 32 000 km^2 characterized by sand dunes, sand sheets and exposed soils. Multi-temporal analysis showed that SDS activity is most frequent during April, June, July and August. Among the tested modelling approaches, the best-performing method reliably identified dust-prone areas, with strong overall classification skill. Precipitation emerged as the dominant environmental control on dust hotspot distribution and variability in the study region.

A study by Ahmady-Birgani (2025) presents a satellite-based framework for identifying and classifying dust-emission hotspots over aeolian landforms using long-term AOD observations processed in Google Earth Engine. Applied to Lake Urmia in Iran, the "Spotfinder" approach distinguishes "coldspots", "hotspots" and "hottestspots" according to the intensity, frequency and trends of dust emissions. The analysis shows a marked environmental shift beginning around 2008, with dust-prone areas expanding from the eastern shoreline to the southern and central basin as the lake dried. By the mid-2010s, shrinking water extent, exposed saline sediments, low precipitation and stronger wind activity had created a persistently dust-active landscape, highlighting dried lakebeds and surrounding margins as rapidly evolving dust sources.

Another satellite-based dust source study developed a 20-year record of blowing dust initiation in south-western North America (Line et al., 2025). This study used geostationary weather satellite imagery from the NOAA Geostationary Operational Environmental Satellite (GOES) system to identify when and where dust plumes first developed. Human analysts reviewed daytime GOES

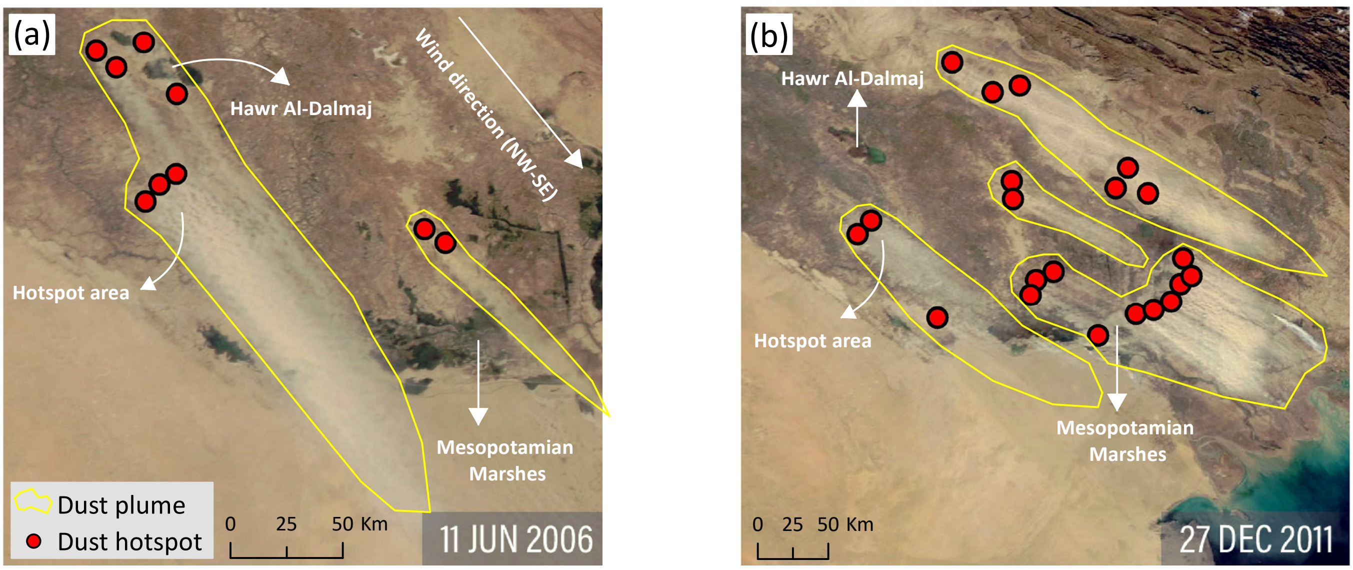

Figure 8. Identification of dust emission hotspots on MODIS true-colour composite imagery using the visual interpretation approach within and around the study area. Examples of two SDSs detected on MODIS Aqua 1:30 p.m. images on (a):11 June 2006 and (b): 27 December 2011.

Source: Al-Hemoud et al. (2024)

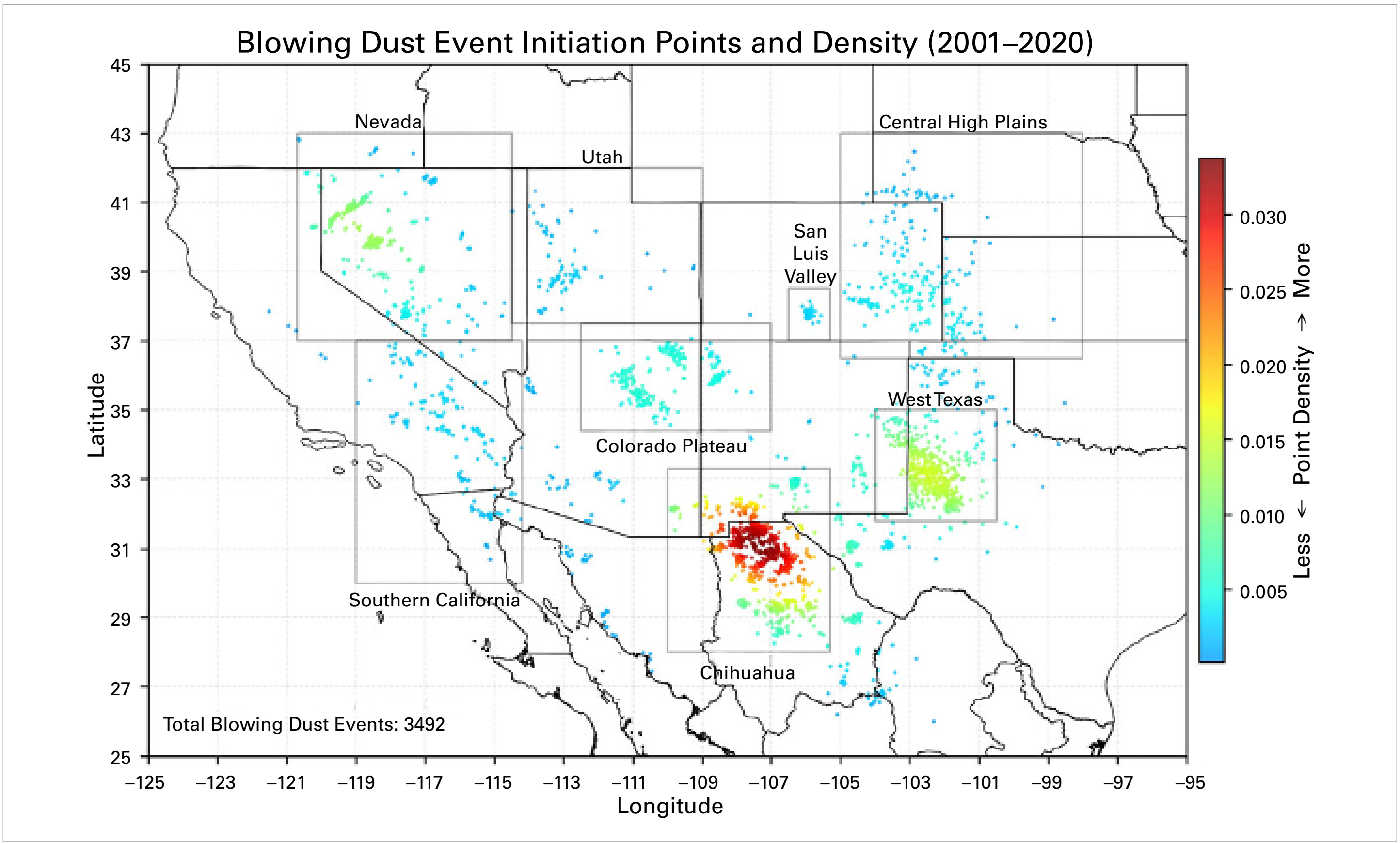

Figure 9. Spatial distribution of blowing dust initiation points identified from GOES imagery across south-western North America from 2001 to 2020. Warmer colours indicate areas with more frequent dust plume initiation.

Source: Third-party map. This map was taken from Line et al. (2025) on 15 May 2026 and may not fully align with United Nations and WMO map guidance.

infrared split window difference imagery from 2001 to 2020 and recorded the initiation time and location of individual blowing dust plumes. A total of 3 492 plumes of blowing dust were identified on 1 066 dust days over the 20-year period. The record shows a clear springtime peak in dust activity, with events typically beginning from late morning into early afternoon as strong winds and boundary-layer mixing increase. The most active source region was the Chihuahuan Desert, especially northern Chihuahua and southern New Mexico, with other notable hotspots in west Texas, north-west Nevada and the Colorado Plateau (Figure 9). Dust activity was especially elevated during major drought periods, including 2002–2003 and 2011–2012, and was reduced during wetter years. Since this study leveraged GOES data and focused on plume initiation, it adds useful spatial and temporal detail that complements surface and polar-orbiting satellite climatology of blowing dust. The dataset supports ongoing and future work on blowing dust detection and forecasting, land surface influences and long-term environmental change.

Surface concentration

A recent study (Proestakis et al., 2025) quantified the particulate matter (PM) mass concentrations (μg m^{-3}) of the submicrometre (fine-mode) and residual supermicrometre (coarse-mode) dust components of the lower troposphere. The analysis was based on a 17-year global dataset (from June 2006 to May 2023) derived from Cloud-Aerosol Lidar and Infrared Pathfinder Satellite Observations (CALIPSO)-Cloud-Aerosol Lidar with Orthogonal Polarization (CALIOP) lidar satellite observations (Proestakis et al., 2024). The study assessed dust PM exposure across major cities and megacities worldwide, characterized by populations greater than 5 million (Figure 10).

The analysis reported the highest near-surface dust mass concentrations mainly for cities across the Middle East, the Indian subcontinent, East Asia, North Africa and the Sahel–Central Africa region. Particularly elevated long-term mean values were reported in Riyadh, Baghdad, Khartoum, Lagos, Karachi, Lahore, the major Indian metropolitan areas (including Delhi, Mumbai, Ahmedabad, Hyderabad and Surat) and key eastern Chinese cities such as Xi'an, Jinan, Nanjing and Tianjin. These findings highlight the widespread influence of mineral dust on air quality (including submicrometre fractions) in densely populated regions and provide a global baseline for assessing population exposure to dust-related particulate pollution.

Radiative assessments

Mineral dust plays a key role in the Earth's radiation budget through its interactions with short-wave (SW) and long-wave radiation (LW), producing both cooling

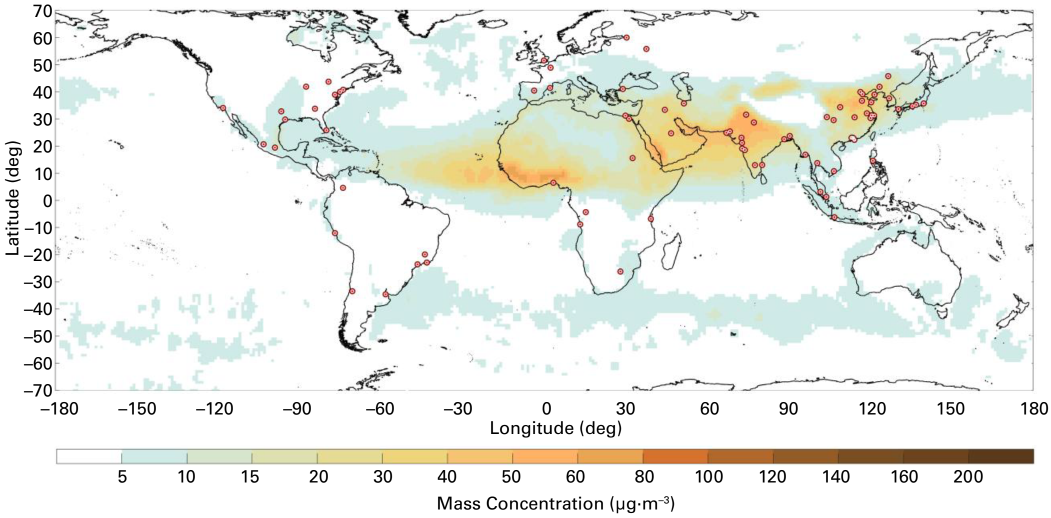

Figure 10. CALIOP-based mean low-level submicrometre-mode dust mass concentration (concentration of particulate matter with a diameter of less than 1 µm (PM_1)) (µg m^{-3}) for the period from June 2006 to May 2023. The circles indicate the location of major cities and megacities worldwide with populations greater than 5 million as of 2018 (United Nations, 2018, 2019).

Source: Third-party map. This map was taken from Proestakis et al. (2025) on 15 May 2026 and may not fully align with United Nations and WMO map guidance.

and warming effects depending on its physical and chemical properties. These radiative impacts are strongly influenced by mineralogical composition, which determines the refractive index and hence the scattering and absorption characteristics of the particles. Dominant silicate minerals, such as quartz and aluminosilicates (for example, illite and kaolinite), are primarily scattering in nature and tend to enhance SW reflection, contributing to surface cooling. In contrast, iron oxide-bearing minerals, particularly hematite and goethite, exhibit significant absorption in the visible and near-infrared wavelength regions, reducing single-scattering albedo and potentially enhancing atmospheric heating within dust layers. Particle size distribution further modulates these radiative effects. Coarse-mode particles typically dominate near-source regions and are efficient at forward scattering. The vertical distribution of dust, in combination with size-resolved mineralogy, is also critical in determining whether radiative effects manifest as surface cooling, atmospheric heating or net regional energy redistribution. Consequently, the overall radiative impact of mineral dust remains highly variable in space and time, reflecting the combined influence of source mineralogy, particle size distribution and atmospheric processing. In this context, mineral dust remains one of the largest uncertainties in the Earth system radiative budget, particularly among natural aerosols.

For more than two decades, the numerical weather prediction and climate modelling community has faced a persistent challenge: limited information is available about the mineralogical composition of airborne dust and its regional variations. A major missing component is information on the spatial variability of the complex refractive index of dust aerosols (Di Biagio et al., 2019; Li et al., 2024), particularly the imaginary part in the visible spectrum, which is largely controlled by iron oxide minerals such as hematite and goethite (Lafon et al., 2006).

Representing mineral dust as composition-resolved mineral components improves Earth system model performance and reduces uncertainty in aerosol radiative effects (Li et al., 2022). Prior to NASA's Earth Surface Mineral Dust Source Investigation (EMIT), global soil mineral datasets were limited to two primary atlases (Claquin et al., 1999; Journet et al., 2014), based on sparse measurements and strong extrapolation from agricultural soils to major arid dust source regions. This introduced substantial uncertainty in prescribed mineralogy, particularly iron oxide content, leading to wide uncertainty in simulated dust SW direct radiative effect (DRE), ranging from net cooling (–0.23 W m^{-2}) to net warming (+0.28 W m^{-2}) (Li et al., 2021). Recent work (Li et al., 2026b) shows that EMIT orbital spectroscopy provides near-global constraints on key dust-source minerals, including hematite and goethite, significantly reducing uncertainty in dust SW DRE by better constraining source-region iron oxide abundance and associated optical properties (Figure 11).

Li et al. (2026a) further demonstrate improved inter-model consistency across Earth system models (ESMs), indicating that a substantial portion of prior model spread was driven by inconsistent mineralogical assumptions. This result is particularly relevant for multi-model assessment frameworks, such as those used in Intergovernmental Panel on Climate Change (IPCC) class evaluations, where structural uncertainty remains a major limitation in constraining aerosol DRE. Overall, EMIT represents a shift towards observation-constrained dust radiative modelling, strengthening confidence in regional and global dust–climate assessments. The success of EMIT has raised expectations that the NASA EAGLE-VSWIR (an imaging spectrometer system), scheduled for launch in 2028, will provide truly global coverage, doubled spatial resolution and regular revisits once every two weeks.

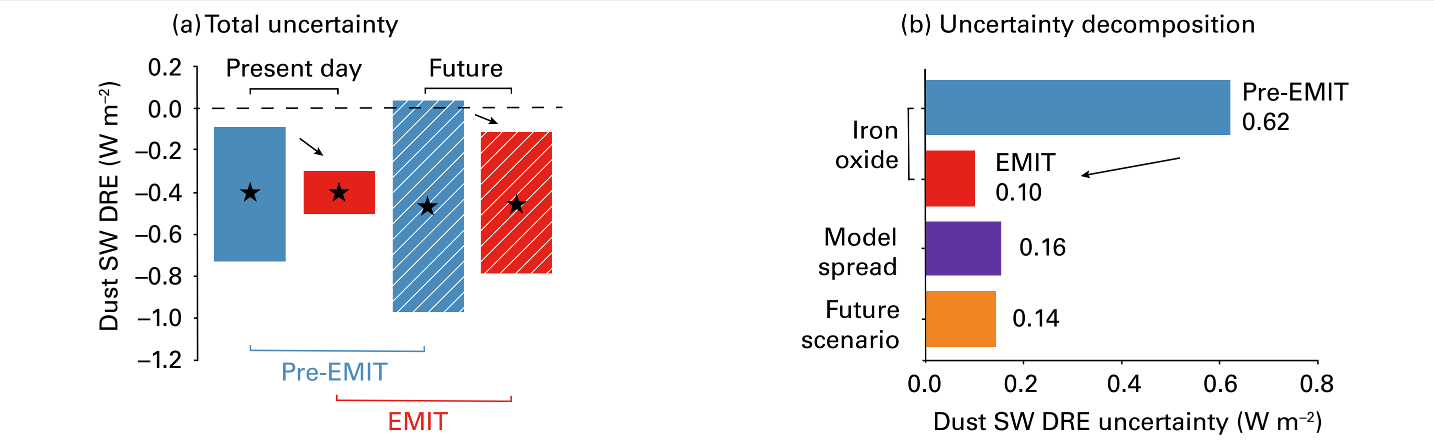

Figure 11. Uncertainty in the dust SW DRE at the top of the atmosphere under all-sky conditions using EMIT data, compared with pre-EMIT estimates. (a) Total uncertainty for present-day (2007–2011) and late 21st-century (2090–2094) climates. (b) Uncertainty attributable to different contributing factors. Future scenarios include the intermediate-mitigation shared socioeconomic pathway SSP2-4.5 and the high-emissions shared socioeconomic pathway SSP5-8.5. See Li et al. (2026b) for details on the methodology and analytical framework.

Source: Li et al. (2026b)

Mineral dust exerts a significant LW radiative heating effect that is substantially underestimated in most climate models. A recent study (Kok et al., 2026) combined observational and modelling constraints on dust size distributions and loading with laboratory-derived optical properties, radiative transfer calculations and meteorological reanalysis data to quantify the global dust LW DRE. Unlike many previous assessments, the analysis explicitly accounted for the contributions of super-coarse dust particles (>10 µm in diameter) and the scattering of LW radiation. The observationally constrained estimate indicates a global annual mean all-sky LW DRE at the top of the atmosphere (TOA) of +0.25 ± 0.06 W m^{-2}, approximately twice the current multi-model mean estimate (~0.13 W m^{-2}) (see Figure 12). This LW effect arises primarily within the atmospheric window (8–14 µm), where outgoing terrestrial radiation is only weakly absorbed by gases, making aerosol–radiation interactions particularly efficient. Dust modifies LW fluxes through two key processes: (i) absorption of upwelling thermal radiation, which is governed by mineral-dependent refractive indices (notably in clay minerals and iron-bearing components), and (ii) scattering of thermal infrared radiation, which redirects upward-emitted radiation back downward, increasing atmospheric absorption and reducing outgoing TOA flux. Importantly, this recent work shows that LW scattering contributes more than half of the total LW DRE, a process neglected in most global radiative transfer schemes that treat dust primarily as a pure absorber in the thermal infrared.

The magnitude of LW heating is strongly controlled by particle size distribution (see Figure 12). Coarse (2.5–10 µm) and super-coarse (>10 µm) particles dominate the LW signal due to their larger extinction efficiencies at thermal wavelengths, with coarse particles contributing roughly two-thirds of the LW DRE and super-coarse particles about one-fifth (see Figure 12). These larger particles are especially effective in enhancing extinction in the atmospheric window, yet are systematically underrepresented in global models due to limitations in emission parameterizations and overly rapid simulated gravitational settling. Vertical structure is also critical: dust layers aloft typically reside above warmer desert and ocean surfaces, where they absorb surface-emitted LW radiation and re-emit it at a lower temperature. This reduces outgoing LW radiation at the top of the atmosphere and produces the strongest LW heating over hot desert source regions.

The combined effect of LW absorption and scattering produces a net atmospheric heating that partially offsets the well-known SW cooling effect of dust and introduces a pronounced regional pattern, with strongest LW warming over source regions such as the Sahara and the Arabian Peninsula. The inclusion of LW scattering and improved representation of coarse and super-coarse dust in radiative transfer schemes reduces the long-standing low bias in model estimates and brings simulations closer to observational constraints.

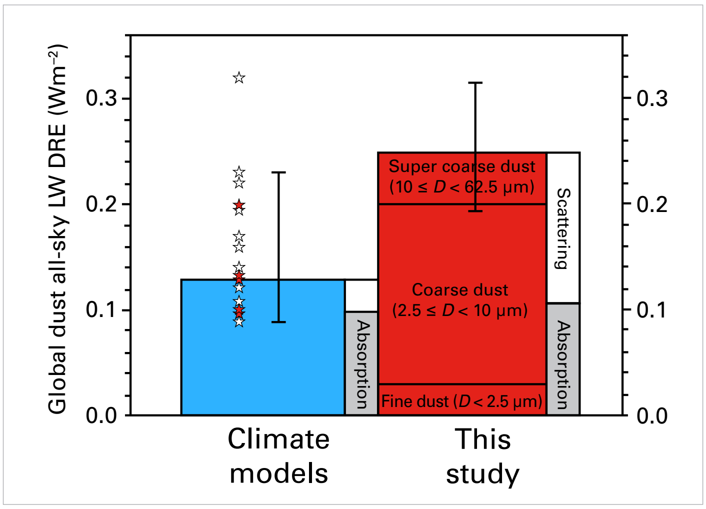

Figure 12. Climate models underestimate the global mean DRE due to dust interactions with LW radiation. A compilation of climate model results (blue bar, with stars representing individual model results) shows a global all-sky TOA LW DRE of 0.13 (0.09–0.23) Wm^{-2}, which is primarily due to LW absorption (grey vertical box), with a small contribution from LW scattering. In contrast, new observationally grounded constraints find the all-sky LW DRE to be almost double that value, 0.25 ± 0.06 Wm^{-2}. More than half of this LW DRE is generated by LW scattering interactions, which are omitted by most global models. Additionally, the majority of the LW DRE is generated by coarse and super coarse dust, which is underestimated by global models.

Source: Kok et al. (2026)

With improved mineralogical constraints and the explicit inclusion of LW scattering, together with a more realistic representation of coarse (2.5–10 μm) and super-coarse (>10 μm) dust in radiative transfer schemes, the long-standing low bias in modelled dust radiative effects is substantially reduced. In addition, the remaining uncertainties are increasingly dominated by dynamical and physical processes, in particular emission parameterizations, vegetation–climate feedback under rising CO_2 and the poorly constrained size distribution and life cycle of coarse and super-coarse particles. These advances have important implications for weather prediction and climate modelling systems where improved representation of SW and LW processes can reduce biases in surface temperature, boundary-layer structure and regional circulation associated with dust outbreaks, thereby enhancing the reliability of both forecast and climate projections in dust-affected regions.

Other news

Transition of the Korean Dust Forecasting System

The Korea Meteorological Administration (KMA) began operational use of its independently developed Korean Integrated Model (KIM) in 2020, running it in parallel with the Met Office Unified Model (UM), which had been in use since 2010. In March 2026, KMA officially ended UM operations and transitioned fully to KIM. As part of this change, the Asian Dust Aerosol Model 3 (ADAM3) forecasting system also shifted from the UM-based framework to the fully coupled KIM-ADAM3 system. The KIM-ADAM3 system has participated in the Beijing Dust Regional Center model intercomparison since 1 April 2026. This transition represents a major step towards full technological independence in SDS forecasting in the Republic of Korea, providing forecasting capabilities tailored to the complex meteorological and topographic conditions of East Asia. Over five years of parallel operation, KIM-ADAM3 demonstrated forecasting performance comparable to UM-ADAM3. Both systems successfully predicted the major dust event of 22–27 March 2025, which originated over southern Mongolia and Inner Mongolia and later affected most of the Republic of Korea. Comparisons with PM_{10} observations at Erenhot in Inner Mongolia showed that KIM-ADAM3 accurately reproduced both the timing and intensity of the event, supporting operational forecasting and decision-making (Figure 13). The successful implementation of KIM-ADAM3 is strengthening the forecasting capacity of the Asian region.

High-latitude dust community updates

Research on high-latitude dust (HLD) continued to expand in 2025, supported by growing international collaboration (including, for example, the Copernicus Atmosphere Monitoring Service National Collaboration Programme (CAMS NCP) and the University of the Arctic (UArctic)) and observational activities across the Arctic and sub-Arctic regions. The 9th High Latitude Dust Workshop, held in Reykjavik, Iceland, in February 2025, brought together approximately 70 participants from 17 countries to discuss recent advances in field observations, remote sensing, modelling, long-range transport, dust–cryosphere interactions and Arctic

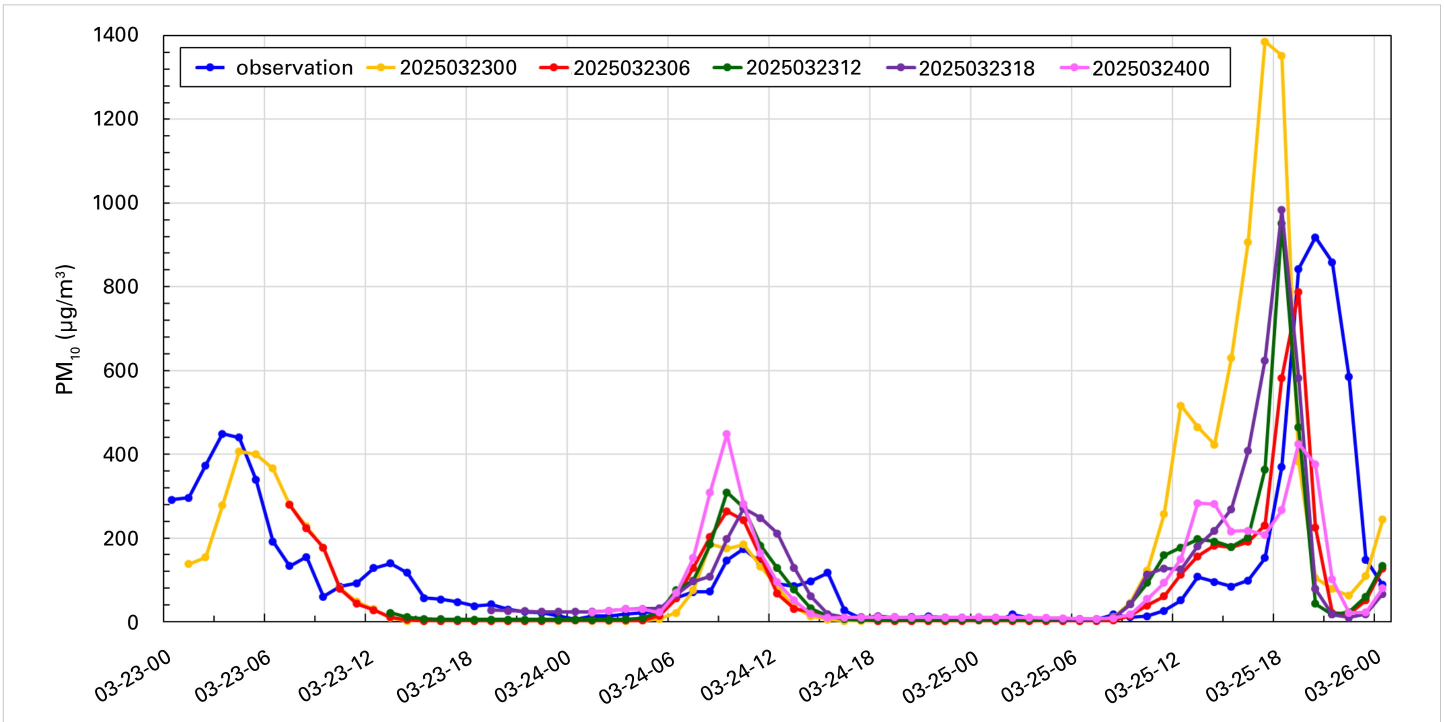

Figure 13. Time series of surface PM_{10} concentrations at the Erenhot station in China comparing ground observations (blue) with the KIM-ADAM3 forecasts. Forecasts initialized at different times are shown in different colours: 25 March 2025, 0000 UTC (yellow); 25 March 2025, 0600 UTC (red); 25 March 2025, 1200 UTC (green); 25 March 2025, 1800 UTC (purple) and 26 March 2025, 0000 UTC (pink).

Source: KMA

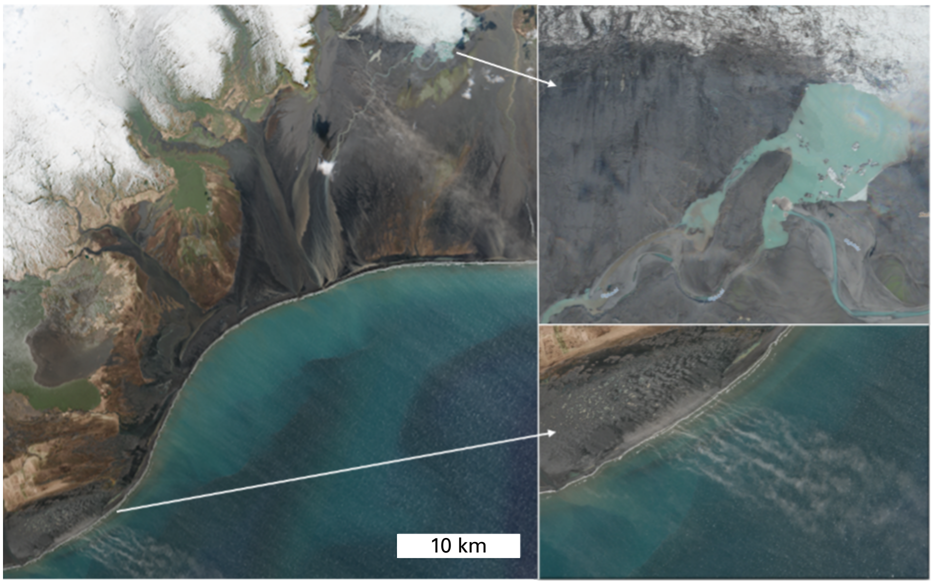

Figure 14. SDSs around Mýrar station in South Iceland on 2 April 2025 (left and lower-right images). The upper-right image shows newly exposed dust sources after glacier melt and small dust plumes from areas on the top of the glacier where dust and ash had been deposited.
Source: Copernicus Data Space Ecosystem

air quality. The workshop highlighted the increasing recognition of HLD as an important component of the global dust cycle and its potential impacts on climate, ecosystems and human activities in polar regions.

New measurements in Iceland further demonstrated the significance of local dust sources (Figure 14). Enhanced monitoring around Iceland's extensive desert areas revealed background particulate matter concentrations comparable to, and at times exceeding, those measured at urban locations. Frequent SDSs produced instantaneous PM_{10} concentrations exceeding 1 000 µg m^{-3}, while newly exposed proglacial areas and dust-rich glacier surfaces were identified as active dust sources. These observations underscore the importance of high-latitude dust emissions in regions undergoing rapid environmental change. The HLD community also continued efforts to engage wider audiences through interdisciplinary initiatives. In 2025, the Dust Forest exhibition in London combined dust science and visual arts to raise awareness of land degradation, desertification, glacier retreat and long-range dust transport.

References

Ahmady-Birgani, H. Conceptualizing Dust Emission Areas and Hotspots over the Aeolian Landforms via Remote-sensing Aerosol Algorithms (Case Study: Lake Urmia, a Major Hypersaline Lake in the Middle East). *Geoscience Letters* **2025**, *12* (1), 28. https://doi.org/10.1186/s40562-025-00400-x.

Al-Hemoud, A.; Naghibi, A.; Hashemi, H. et al. Dust Source Susceptibility in the Lower Mesopotamian Floodplain of Iraq. *Remote Sensing Applications: Society and Environment* **2024**, *36*, 101355. https://doi.org/10.1016/j.rsase.2024.101355.

Amiridis, V.; Marinou, E.; Tsekeri, A. et al. LIVAS: A 3-D Multi-wavelength Aerosol/Cloud Database Based on CALIPSO and EARLINET. *Atmospheric Chemistry and Physics* **2015**, *15* (13), 7127–7153. https://doi.org/10.5194/acp-15-7127-2015.

Claquin, T.; Schulz, M.; Balkanski, Y. Modeling the Mineralogy of Atmospheric Dust Sources. *Journal of Geophysical Research: Atmospheres* **1999**, *104* (D18), 22243–22256. https://doi.org/10.1029/1999JD900416.

Darvishi Boloorani, A.; Soleimani, M.; Papi, R. et al. Global Map of Characterized Dust Sources Using Multisource Remote Sensing Data. *Scientific Reports* **2025**, *15* (1), 29805. https://doi.org/10.1038/s41598-025-14794-3.

Di Biagio, C.; Formenti, P.; Balkanski, Y. et al. Complex Refractive Indices and Single-scattering Albedo of Global Dust Aerosols in the Shortwave Spectrum and Relationship to Size and Iron Content. *Atmospheric Chemistry and Physics* **2019**, *19* (24), 15503–15531. https://doi.org/10.5194/acp-19-15503-2019.

Doermann, L. *Dust Storm Sweeps through Iraq*; National Aeronautics and Space Administration (NASA) Earth Observatory, 2025. https://science.nasa.gov/earth/earth-observatory/dust-storm-sweeps-through-iraq-154186/.

Earth Cloud Aerosol and Radiation Explorer (EarthCARE). *Atmospheric Lidar (ATLID)*; Japan Aerospace Exploration Agency (JAXA) Earth Observation Research Center (EORC). https://www.eorc.jaxa.jp/EARTHCARE/about/inst_atlid_e.html.

Gui, K.; Zhang, X.; Che, H. et al. Advancing Operational Global Aerosol Forecasting with Machine Learning. *Nature* **2026**, *651* (8106), 658–665. https://doi.org/10.1038/s41586-026-10234-y.

Journet, E.; Balkanski, Y.; Harrison, S. P. A New Data Set of Soil Mineralogy for Dust-cycle Modeling. *Atmospheric Chemistry and Physics* **2014**, *14* (8), 3801–3816. https://doi.org/10.5194/acp-14-3801-2014.

Kok, J. F.; K. Gupta, A.; Evan, A. T. et al. Desert Dust Exerts Twice the Longwave Radiative Heating Estimated by Climate Models. *Nature Communications* **2026**, *17* (1), 3191. https://doi.org/10.1038/s41467-026-70952-9.

Lafon, S.; Sokolik, I. N.; Rajot, J. L. et al. Characterization of Iron Oxides in Mineral Dust Aerosols: Implications for Light Absorption. *Journal of Geophysical Research: Atmospheres* **2006**, *111* (D21). https://doi.org/10.1029/2005JD007016.

Li, L.; Mahowald, N. M.; Miller, R. L. et al. Quantifying the Range of the Dust Direct Radiative Effect Due to Source Mineralogy Uncertainty. *Atmospheric Chemistry and Physics* **2021**, *21* (5), 3973–4005. https://doi.org/10.5194/acp-21-3973-2021.

Li, L.; Mahowald, N. M.; Kok, J. F. et al. Importance of Different Parameterization Changes for the Updated Dust Cycle Modeling in the Community Atmosphere Model (Version 6.1). *Geoscientific Model Development* **2022**, *15* (22), 8181–8219. https://doi.org/10.5194/gmd-15-8181-2022.

Li, L.; Mahowald, N. M.; Gonçalves Ageitos, M. et al. Improved Constraints on Hematite Refractive Index for Estimating Climatic Effects of Dust Aerosols. *Communications Earth & Environment* **2024**, *5* (1), 295. https://doi.org/10.1038/s43247-024-01441-4.

Li, L.; Mahowald, N. M.; Liu, X. et al. Modeling Large Dust Aerosols in the Community Earth System Model Version 2 (CESM2). *Journal of Advances in Modeling Earth Systems* **2026a**, *18* (4), e2025MS005420. https://doi.org/10.1029/2025MS005420.

Li, L.; Mahowald, N. M.; Miller, R. L. et al. Global Mineral Constraints on Dust Shortwave Radiative Effects. *Nature Geoscience* **2026b**, 1–7. https://doi.org/10.1038/s41561-026-01996-1.

Line, W. E.; Turner, J. D.; Bleiweiss, M. P. et al. GOES-based Trends in Blowing Dust Initiation across Southwestern North America, 2001–20. *Journal of Applied Meteorology and Climatology* **2025**, *64* (12), 1833–1850. https://doi.org/10.1175/JAMC-D-25-0035.1.

Proestakis, E.; Gkikas, A.; Georgiou, T. et al. A Near-global Multiyear Climate Data Record of the Fine-mode and Coarse-Mode Components of Atmospheric Pure Dust. *Atmospheric Measurement Techniques* **2024**, *17* (12), 3625–3667. https://doi.org/10.5194/amt-17-3625-2024.

Proestakis, E.; Papachristopoulou, K.; Georgiou, T. et al. Atmospheric Dust and Air Quality over Large-cities and Megacities of the World. *Atmospheric Chemistry and Physics* **2025**, *25* (21), 14777–14823. https://doi.org/10.5194/acp-25-14777-2025.

Standardised Precipitation-Evapotranspiration Index (SPEI) Global Drought Monitor. https://spei.csic.es/map/maps.html.

United Nations, Department of Economic and Social Affairs, Population Division. *The World's Cities in 2018*; United Nations, 2018. https://www.un.org/development/desa/pd/content/worlds-cities-2018-data-booklet.

United Nations, Department of Economic and Social Affairs, Population Division. World Urbanization Prospects: The 2018 Revision; United Nations, 2019. https://www.un.org/development/desa/pd/content/world-urbanization-prospects-2018-revision.

Wang, J.; Hua, C. An Artificial Intelligence Model for Sand and Dust Storm Forecast Driven by AI Weather Forecasts. *npj Clean Air* **2026**, *2* (1), 10. https://doi.org/10.1038/s44407-025-00048-z.

World Meteorological Organization (WMO). *WMO Airborne Dust Bulletin, No. 9*; WMO: Geneva, 2025.

WMO SDS-WAS websites and contacts

WMO SDS
https://wmo.int/topics/sand-and-dust-storms
Email: gaw@wmo.int

SDS-WAS
https://community.wmo.int/site/knowledge-hub/governance/research-board/environmental-pollution-and-atmospheric-chemistry-scientific-steering-committee-ssc-epac/sand-and-dust-storms-warning-advisory-and-assessment-system
Email: gaw@wmo.int

Regional Centre for Northern Africa, Middle East and Europe (NAMEE):
http://dust.aemet.es Email: dust@aemet.es

Regional Centre for Asia:
http://www.asdf-bj.net/ Email: wmc-bj@cma.gov.cn

Regional Centre for the Americas:
http://sds-was.cimh.edu.bb/ Email: asealy@cimh.edu.bb

Regional Centre for Gulf Cooperation Council (GCC) Countries:
http://dust.ncm.gov.sa/ Email: sdsc@ncm.gov.sa

Editorial Board

All authors (in alphabetical order)

Randa Ghrib Abdullah, Hesam Ahmady Birgani, Marwa F. M. Ali, Ali Al-Hemoud, Pavla Dagsson-Waldhauserová, Emanuele Emili, Jerónimo Escribano, Rania Ezzeldeen, Nourhan Elshafeey, Diana Francis, Manar Gamal Ghanem, Thomas Gill, Hailin Gui, Ke Gui, Miguel Hortelano, Cong Hua, Maki Kikuchi, Migyeong Kim, Jasper Kok, Takuji Kubota, Mona M. Labib, Longlei Li, William Line, Antonios Mekhiel, Ron L. Miller, Hiroshi Murakami, Masataka Muto, Mi Eun Park, Hervé Petetin, Emmanouil Proestakis, Reham Rabie, Zeinab Salah, Jikang Wang, Lamiaa Salim Yousif

World Meteorological Organization wmo.int

JN 26212